Force interaction of high pressure glow discharge with fluid flow for active separation control

Subrata Roy[a)]
Computational Plasma Dynamics Laboratory, Mechanical Engineering, Kettering University, Flint, Michigan 48504

Datta V. Gaitonde
Computational Sciences Branch, Air Vehicles Directorate, Air Force Research Laboratory, Wright Patterson AFB, Ohio 45433

(Received 12 October 2005; accepted 19 December 2005; published online 24 February 2006)

Radio frequency based discharges at atmospheric pressures are the focus of increased interest in aerodynamics because of the wide range of potential applications including, specifically, actuation in flows at moderate speeds. Recent literature describing promising experimental observations, especially on separation control, has spurred efforts in the development of parallel theoretical modeling to lift limitations in the current understanding of the actuation mechanism. The present effort demonstrates higher fidelity first-principle models in a multidimensional finite-element framework to predict surface discharge-induced momentum exchange. The complete problem of a dielectric barrier discharge at high pressure with axially displaced electrodes is simulated in a self-consistent manner. Model predictions for charge densities, the electric field, and gas velocity distributions are shown to mimic trends reported in the experimental literature. Results show that a residual of electrons remains deposited on the dielectric surface downstream of the exposed powered electrode for the entire duration of the cycle and causes a net electric force in the direction from the electrode to the downstream surface. For the first time, results document the mitigation process of a separation bubble formed due to flow past a flat plate inclined at 12° angle of attack. This effort sets the basis for extending the formulation further to include polyphase power input in multidimensional settings, and to apply the simulation method to flows past common aerodynamic configurations. © *2006 American Institute of Physics*. [DOI: 10.1063/1.2168404]

I. INTRODUCTION

Various experimental efforts[1–6] have demonstrated the feasibility of utilizing dielectric barrier discharge (DBD) at high pressure to inhibit phenomena such as stall on airfoils, thus improving their lift-drag curves. A particularly attractive feature of these plasma-based devices is their capacity to operate at atmospheric conditions without uncontrolled macroscopic breakdown. Experimental efforts have identified many of the key parameters, most prominent among which are features of the geometric configuration and the form of the applied excitation.

A schematic of a typical actuator is shown in Fig. 1. Two electrodes are employed: the first exposed to the flow and the second embedded in the dielectric and displaced in the streamwise direction relative to the exposed electrode. The surface discharge so created contrasts with the volumetric effect observed when the electrodes are separated by the fluid. Typically, the actuator is excited by powering the exposed electrode at radio frequency (rf) voltages, while the embedded electrode is grounded. In another arrangement, both electrodes are powered with signals separated by a beat frequency. The excitation induces a complex unsteady interaction between the two electrodes and the fluid, details of which depend on frequency, voltage, geometric configuration, and dielectric constants of the media. In the surface discharge, within a very short time after breakdown, the charge buildup at the dielectric surface sets off microdischarges of nanosecond duration, limiting the electric field at the location of the microdischarge such that the charge current at this position is cut off. Experimental evidence shows that there is no runaway state for the parameters under consideration and that an asymptotic (quasi) periodic state is reached, with a dominant frequency that is locked to the input perturbation. For a given interelectrode distance, as the applied voltage becomes sufficiently large, the dielectric surface adjacent to the rf electrode produces a barrier discharge, which weakly ionizes the surrounding gas. The combination of electrodynamic body force and collisional processes, whose detailed mechanics remains a matter of current research, ultimately transfers momentum acquired from the electric field by the charged particles to the neutrals which are the primary species.

The advantages of dielectric barrier-based discharges include an absence of moving parts, rapid on-off features, and the ability to apply body forces in a relatively precise manner by deploying advanced electromagnetic technology. The devices are thus optimally suited for flow control in wall layers or separated layers[1–10] The main parameters applied in experimental observations include peak-to-peak voltage between 2–20 kV at 1–50 kHz rf, which are suitable for actuation at atmospheric pressure at low speeds to $O(10)$ Torr at high speeds. Specifically, at high pressures the fluid is

[a)]Electronic mail: sroy@kettering.edu

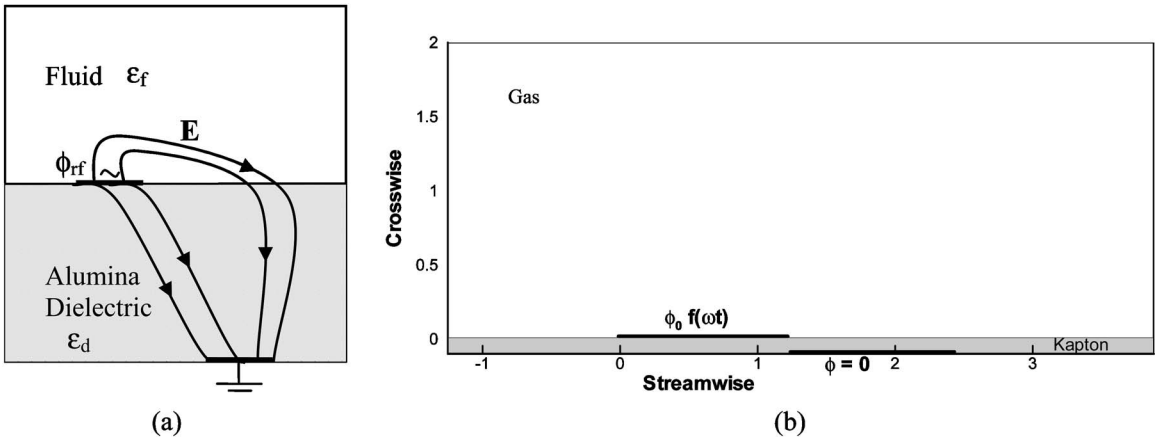

FIG. 1. Schematic of the rf induced dielectric barrier discharge device. The shaded region is an insulator with embedded (grounded, $\phi=0$) and exposed [powered, ϕ_0 f(ωt)] electrodes shown in thick solid line segments. (a) Square (S) geometry with alumina insulator. (b) Rectangular (R) geometry with Kapton insulator.

highly collisional, inducing an efficient momentum transfer between charged and neutral species.

The collisional rf sheath dynamics of near-surface regions is fundamentally different from that under direct current (dc) and/or collisionless conditions and substantially more difficult to simulate because of their unsteady nature. While dc-based methods are a useful study for energy interactions of an already ionized flow, recent literature[11–13] shows that energy budgets will depend crucially on dynamic nonequilibrium ionization techniques. The load factor for dc sheath application is of order 1, far from the most energy efficient Stoletow point, thus generally unsuitable for ionization purposes. While the earliest atmospheric glow discharge research by von Engle *et al.*[14] was published over 70 years ago, recent experimental successes of rf-induced glow discharge using air at atmospheric condition[1–6] have triggered tremendous interest in the electro-gas dynamic flow control and energy management community. Microfilaments of nanosecond duration with many current pulses in a half cycle maintain the optical glow in dielectric barrier discharge (typically, it is the light emission spectrum that remains diffused to create a uniform glow). The small time scale of the discharge limits charge transport and induces minimal heating of the bulk gas.[9,15] Thus, most of the electric energy is utilized for exciting the carrier gas, resulting in efficient applications to boundary layer flow actuation. Interestingly, one atmosphere uniform glow discharge plasma (OAUGDP)[1,4] also shows similar flow-induction phenomenology, but apparently without the filamentation. Henceforth, we will use the term DBD loosely to address optical glow discharge at high pressures.

The typical distance between dielectric barrier discharge (DBD) electrodes is ~0.1 mm in plasma displays, over 1 mm in ozone generators, to several centimeters in CO_2 lasers.[15] It has been observed that in some gases (e.g., helium) the discharge glow is stable, whereas for the same interelectrode gap and pressure air, nitrogen, oxygen, and argon transition into an unstable filamentary discharge.[15] While there are two types of DBD, namely volume discharge between two parallel plates and surface discharge over a dielectric boundary, this study focuses on the latter.

Despite the extensive recent experimental data on atmospheric DBD interactions for flow actuation, the theoretical modeling effort is still in its infancy. These few efforts span a range of phenomenological to rudimentary first-principle-based methods.[4,5,7–10,16] For example, Roth[4] utilized a postulated balance between the electrostatic force and the hydrodynamic force to estimate the induced gas velocity. Enloe *et al.*[5] have analytically shown in a simple one-dimensional axisymmetric configuration that two-dimensional electric force modeling is essential to the understanding of the glow discharge flow actuation process. For accuracy and fidelity, it is imperative that the force model be derived from first principles through a simulation of the elementary mechanisms that yield the discharge. Shyy *et al.*[7] developed an empirical model based on pictures of the glow. Although rudimentary, it provides a spatial variation of force through an assumed triangular distribution of the electrostatic body force downstream of the electrode. Recently, Gaitonde *et al.*[16] parametrized the force direction, and incorporated it into fully 3D direct numerical simulations to described the response of the flow past a stalled NACA 0015 airfoil at 15° angle of attack.

For accuracy and fidelity, however, it is imperative that the force model be derived from first principles through a simulation of the elementary mechanisms that yield the discharge characteristics and flow actuation similar to that found in the experiments. Roy and Gaitonde demonstrated such a model, first for volume discharge between two dielectric coated electrodes[8] and then for capturing effects of surface discharge on quiescent helium gas,[9,10] using a finite-element-based multidimensional multifluid formulation of plasma sheath at atmospheric conditions. While the first model was relatively basic, the two-dimensional model of high pressure surface glow discharge documented a consistent first-principles formulation of charge and neutral number densities, their momentum dynamics, electrostatic field, and potential distribution for an asymmetric DBD configuration. The model treated the insulator and the gas simultaneously and integrated the Poisson equation into the charge and gas dynamics. Simulations showed reasonable comparison with

reported rf glow discharges[17] in partially ionized helium gas between two insulated electrodes. The current effort, focused as it is on surface discharges which have proven more attractive in flow control, is a logical next step in the evolution of computational methods for high pressure glow discharges.

The present paper reports the first two-dimensional tightly coupled first-principles model demonstrating control of a separated flow at atmospheric pressure. The methodology ensures a consistent calculation of charge and neutral number densities, their momentum dynamics, electric field, and potential distribution. The formulation is anchored in an efficient, robust, and versatile module-based finite-element code, to facilitate the prediction of the electric field from the charge distribution computed from the grounded and applied rf potential and the dielectric properties of insulator and gas media. The electric force, computed as a product of self-consistent charge and electric field, is employed to calculate the flow actuation effect. For simplicity, here again helium is used as a carrier gas because its plasma coefficients and chemistry are known. These self-consistent simulations lay the foundation for a detailed analysis of the interaction between charged and neutral particles in the important situation where separation is affected. This facilitates a more insightful understanding of the complex relation between the body force, inertial, viscous, and pressure fields to augment experimental observations. This work also provides a basis through which future efforts can investigate the impact of dimensionless parameter variation, particularly of the Reynolds number, to yield guidance on the potential scalability of these devices.

II. MODEL DETAILS

The following two-dimensional three-species collisional plasma-sheath model is solved:

$$\text{Charge continuity:} \quad \frac{\partial n_\alpha}{\partial t} + \frac{\partial n_\alpha V_{\alpha j}}{\partial x_j} = n_e z - r n_e n_i, \tag{1a}$$

$$\text{Charge momentum:} \quad n_\alpha V_{\alpha j} = -\,\mathrm{sgn}(e) n_\alpha \mu_\alpha \frac{\partial \phi}{\partial x_j} - D_\alpha \frac{\partial n_\alpha}{\partial x_j}, \tag{1b}$$

$$\text{Potential:} \quad \varepsilon\left(\frac{\partial^2 \phi}{\partial x_j^2}\right) = e(n_e - n_i). \tag{2}$$

The charge particle $\alpha = e, i$ distributions are considered non-Maxwellian. The electron temperature is nearly uniform at 1 eV = 11 600 K and the ions and neutrals are in thermal equilibrium at 300 K. The working gas, helium, is maintained at bulk pressure $p = 300$ Torr and temperature $T = 300$ K. For the operating condition of interest, the inertia terms are small relative to the effect of the electrical field and collisional interactions, and thus neglected. The collisional momentum exchange is vital to the charge-to-neutral momentum transfer.

The electron diffusion is obtained from the Einstein relation, $D_e = (T_e/e)\mu_e$, where T_e is the energy in electron volts, e is the elementary charge, ε is the permittivity, and $\mu_e = e/(m_e \nu_{eh})$ is mobility of an electron, where $\nu_{eh} \sim \nu_{en} \approx 10^{12}$/s is the electron-neutral collision frequency. In this context, we note that transport properties, which have been taken from the literature, are to be viewed as nominal values facilitating the development of the numerical framework, rather than to fill gaps in current thermo-chemical data for the environment of interest. In this same vein, D_i is the ion diffusion[18] in cm^2/s at 300 K, and the ion mobility μ_i is given as[19]

$$\begin{aligned} p\mu_i &= 8 \times 10^3 (1 - 8 \times 10^{-3} E/p)\ \mathrm{cm^2\ V^{-1}\ s^{-1}\ Torr}, \\ &\quad \text{for } E/p \leqslant 25\ \mathrm{V\ cm^{-1}\ Torr^{-1}}, \\ p\mu_i &= \frac{4.1 \times 10^4}{\sqrt{E/p}}\left(1 - \frac{27.44}{(E/p)^{3/2}}\right)\ \mathrm{cm^2\ V^{-1}\ s^{-1}\ Torr}, \\ &\quad \text{for } E/p > 25\ \mathrm{V\ cm^{-1}\ Torr^{-1}}, \end{aligned} \tag{3}$$

where $E = \sqrt{E_x^2 + E_y^2}$ is the electric field magnitude with components $E_j = -\partial\phi/\partial x_j$ and p is the gas pressure. The index j takes the values x and y. Note that the ion mobility is based on an empirical relation that contains the electric field and pressure, assuring consideration of collisional effects. However, quantitative results will depend on the nominally chosen values. The ionization rate z for helium gas used here is[7–9]

$$\begin{aligned} z &= A \exp\left(\frac{-B}{(E/p)^{0.4}}\right) p\mu_e E\ \mathrm{s^{-1}}; \\ A &= 4.4\ \mathrm{cm^{-1}\ Torr^{-1}} \text{ and } B = 14\ [\mathrm{V/(cm\ Torr)}]^{0.4}, \end{aligned} \tag{4}$$

where n_e is the electron number density. The coefficient of two-body and three-body recombination on the right-hand side of Eq. (1a) is given as[20] $r = [V_{e\mathrm{th}} \sigma_{ei}^r (V_{e\mathrm{th}})]$ cm^3/s. Here, $V_{e\mathrm{th}}$ is the electron thermal velocity and σ_{ei} is the electron-ion collision cross section. For simplicity, we have negligible secondary emission at this operating frequency. The following boundary conditions are maintained: At the electrode, we maintain $D_e(\partial n_e/\partial x_2) = n_e \mu_e (\partial\phi/\partial x_2) - \sigma n_e V_{e\mathrm{th}}$, and $D_i(\partial n_i/\partial x_2) = 0$. The factor σ is set to 0 or 1 depending on the positive or negative value of the exposed electrode in the rf cycle.

Importantly, any balance between the electrostatic and fluid dynamic pressure gradients cannot be guaranteed for a fundamentally unsteady process. We use the electrodynamic body force $e(n_i\text{-}n_e)\mathbf{E}$ (although no Lorentz force is present, the force is created by charge transport) to compute the averaged velocity of the working fluid is based on the following continuity and momentum equations:

$$\partial\rho/\partial t + \partial\rho V_{fj}/\partial x_j = 0, \tag{5a}$$

$$\frac{\partial V_{fj}}{\partial t} + V_{fl}\frac{\partial V_{fj}}{\partial x_l} = \frac{\varpi}{\rho} e(n_i - n_e) E_j - \frac{RT}{\rho}\frac{\partial \rho}{\partial x_j} + \frac{\partial}{\partial x_l}\tau_{jl}, \tag{5b}$$

where $\tau_{jl} = \mu/\rho(\partial V_{fl}/\partial x_j + \partial V_{fj}/\partial x_l) - \frac{2}{3}(\mu/\rho)\partial V_{fk}/\partial x_k \delta_{jl}$, with μ as the gas viscosity ($=2.066 \times 10^{-5}$ N s/m^2) and δ_{jl} is the Kronecker delta. Helium is assumed as an ideal gas. The factor ϖ is introduced to modulate the effect of electric field.

The multiscale ionized gas (MIG) flow code was used to solve Eqs. (1a), (1b), (2)–(4), (5a), and (5b). MIG has a module-based computational platform that implements the high-fidelity finite-element (FE) procedure adapted from fluid dynamics to overcome the stiffness of the equations generated by multispecies charge separation phenomena. This code has been used and validated for several fluid dynamics,[21] ionized gas,[8–10,22] and micro/nanoscale[23,24] flow problems. FE techniques are especially suitable for their adaptability to arbitrary multidimensional geometries and boundary conditions. Here, a 2D biquadratic FE formulation is employed along with fourth-order Runge-Kutta time marching to solve the continuity and momentum equations for all species and fluid. The solution process consists of two steps. First, using Eqs. (1a), (2), and (3), a global matrix is formed and solved simultaneously, obviating the need for any special subiteration for the Poisson solver. The charge density and electric field thus calculated are then used in Eqs. (5a) and (5b) to predict the fluid velocity. The Galerkin weak statement associated with a variational integral underlines the development of this numerical algorithm. Note that the selection of a test function orthogonal to the trial function in Galerkin formulations guarantees the minimization of error,[25] making it better suited for these problems. Details of the MIG code are reported elsewhere (for example, see Refs. 20 and 21). For the species equations (1)–(4), a solution adaptive time scale of up to 100 times the dielectric relaxation time scale[26] is adopted to calculate the charge separation and electric field up to a periodic asymptote. The gas equations (5a) and (5b) are then solved using the volume specific electrodynamic body force to predict the fluid velocity and continuity evolving in time with the flow time scale of ~ms. The solution of the Newton-Raphson iteration is converged at any given time step when the maximum value of the residual, relative L_2 norm for each of the state variables, becomes smaller than a chosen convergence criterion of 10^{-4}.

III. PROBLEM DESCRIPTION

Two distinct geometries denoted as S (square) and R (rectangle) are simulated.

A. Geometry S

The two-dimensional computational domain $(x,y: 0,1$ cm) consists of a lower half ($y: 0,\ 0.5$ cm) insulator with dielectric constant ε_d, and a upper half filled with inert helium gas of $\varepsilon_f=1.0055\ \varepsilon_0$, where ε_0 is permittivity of vacuum. Inside the insulator the current due to motion of charged particles is forced to zero, while the displacement current is balanced with the total current at the gas-dielectric boundary. The bottom encapsulated electrode is grounded and a rf alternating frequency of 5 kHz with peak-to-peak potential of 2 kV is imposed at the top electrode. Each electrode is infinitesimally thin and 2 mm long. In order to identify the effect of electrode configuration two different electrode arrangements were simulated. In the first, denoted as S-1, the two electrodes were kept vertically aligned. Hereafter, we will denote this as the symmetric configuration. In the second case, denoted as S-2, the electrodes are offset horizontally by 2 mm. This will be noted as the asymmetric configuration. The gas is assumed initially stagnant ($V_{fj}=0$). The solutions are verified by qualitative comparison with the reported results. The results are then employed to explore the enhancement of near wall fluid velocity.

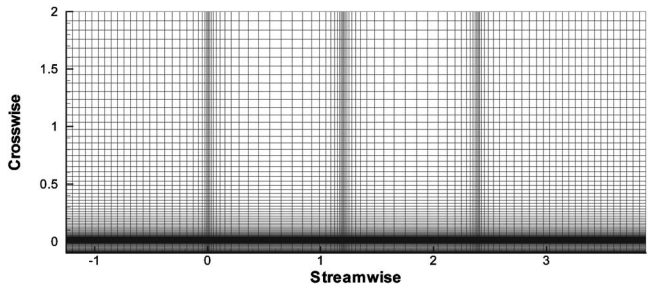

FIG. 2. Representative computational mesh shows highly nonuniform nature.

B. Geometry R

The two-dimensional computational domain $(-1.252, 3.880$ cm$)\times(-0.1, 2.0$ cm$)$ consists of a Kapton polyimide insulator in the lower half ($y: -0.1, 0$ cm) with a dielectric constant $\varepsilon_d=3.5\ \varepsilon_0$ and the upper half ($y: 0, 2$ cm) filled with inert helium gas of $\varepsilon_f=1.0055\ \varepsilon_0$, where ε_0 is permittivity of vacuum. Inside the insulator the current due to motion of charged particles is forced to zero while the displacement current is balanced with the total current at the gas-dielectric boundary. The schematic in Fig. 1 shows two electrodes in which the bottom electrode is grounded and a rf alternating frequency of 5 kHz with rms potential of 2 kV is imposed at the top electrode. Each electrode is infinitesimally thin and 1.2 cm long. They are vertically displaced by 1 mm with no horizontal overlap. The highly stretched representative computational mesh shown in Fig. 2 consists of 51×53 two-dimensional biquadratic Lagrange finite elements. The insulator material is modeled using 12×53 biquadratic elements. The nodes are attracted toward the wall and electrode edges for capturing better solution details. The highest and lowest elemental aspect ratios are approximately 90 and 10, respectively. In order to identify the charge characteristics and its effect on gas flow, two different simulations were performed on a single geometric configuration with an asymmetrically displaced electrode-pair arrangement. In the first, no gas velocity was imposed, i.e., quiescent flow. Hereafter, we will denote this as case R-1. In the second, an upstream flow of 10 m/s was imposed at $x=-1.252$ cm with an angle of attack (AOA) of $+12°$. This will be noted as case R-2.

For all simulations (S-1, S-2, R-1, and R-2) electrons are assumed to be isothermal at the boundary and maintained at 1 eV (~11 600 K) while the ions are cold (300 K) at 300 Torr. The electron flux at the exposed electrode is based on the electron thermal velocity and is neglected unless directed toward the wall. Homogeneous Neumann boundary conditions are applied for all other variables at other boundaries. Zero flux, i.e., homogeneous Neumann boundary con-

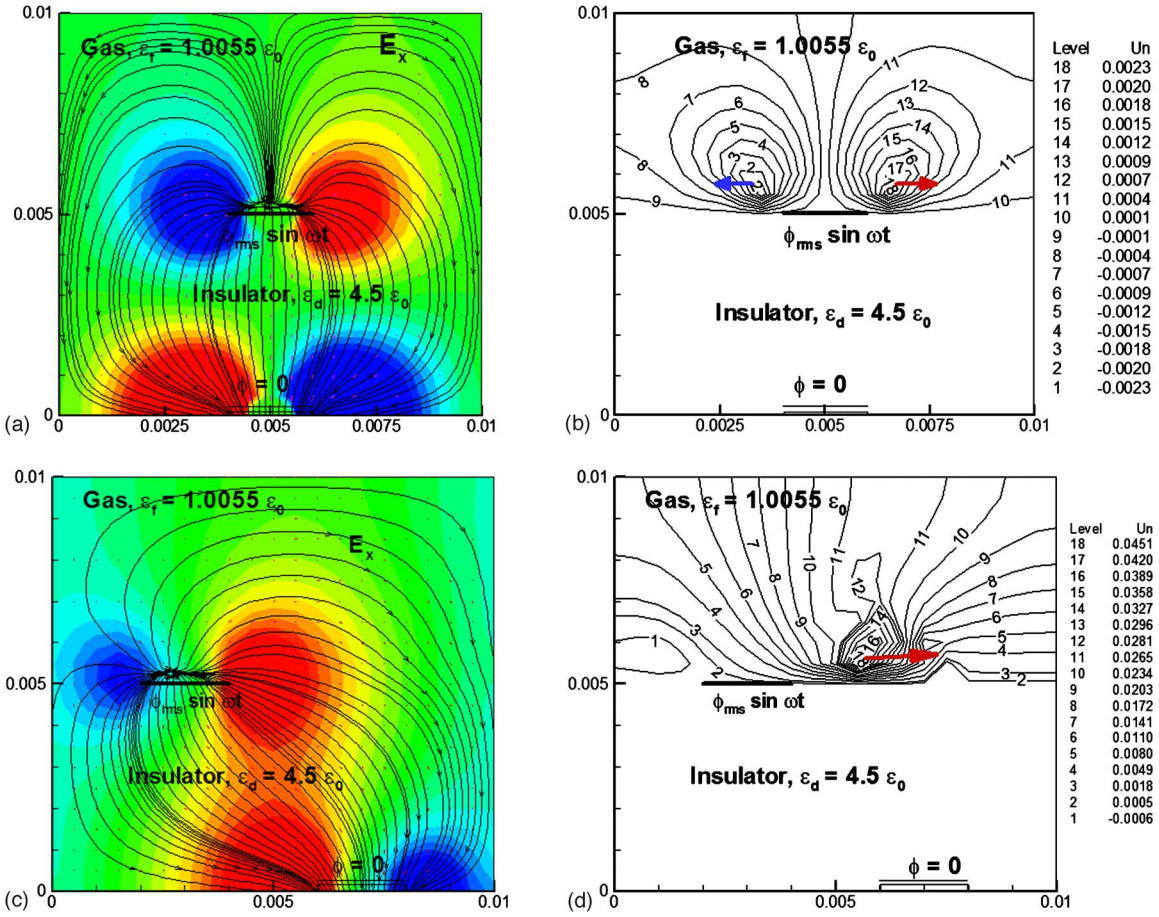

FIG. 3. (Color online) (a), (b) Solution for symmetric configuration. (a) Computed axial electric field contours with embedded electric field lines. (b) Streamwise velocity contours calculated from the electric field in (a) shows counteracting flow field. (c), (d) Solution for asymmetric configuration. (c) Computed axial electric field contours with embedded electric field lines. (d) Streamwise velocity contours calculated from the electric field in (c) shows positive flow field.

ditions, are applied at all other boundaries. The solutions are verified by qualitative comparison with the reported results. The results are then employed to explore the enhancement of near-wall fluid velocity. No-slip gas velocity boundary condition is imposed for all cases. Also, the insulator is considered impermeable to gas.

IV. RESULTS AND DISCUSSION

Figure 3 displays several features of the numerical predictions on both the symmetric S-1 and asymmetric S-2 configurations. For S-1, Fig. 3(a) shows the axial electric field contours with embedded electric field lines computed for the symmetric configuration (at $\sim\pi/2$ radians). The electric field lines trace the vector path moving in a trajectory from the exposed instantaneous anode to the grounded cathode inside the dielectric in a symmetric fashion. The ions travel along these repelling field lines of equal strength pushing outward from the center above the rf electrode inducing the neutral gas particles to follow suit. The net effect is clearly seen in the streamwise gas velocity contours in Fig. 3(b) calculated from the electric field depicting a counteracting flow field that reduces the neutral gas density in the region above the exposed (rf) electrode. An interesting outcome is that the fluid over the electrode will respond to this pulsating field by forming a jet, whose oscillations will depend on fluid inertia and the instantaneous polarity.

However, this characteristic behavior changes when the embedded electrode is displaced axially relative to the exposed electrode. Figure 3(c) plots the instantaneous (at $\sim\pi/2$ radians) axial electric field distribution for an exposed anode and a grounded cathode in asymmetric configuration. The magnitude of the axial field shows a large round peak (in red) at the right of the anode and a small negative (in blue) just left of the anode. The electric field lines overlaid on this clearly represent a directional bias toward the right. The dominant acceleration of ions in this direction occurs along these lines, leaving only a relatively smaller regime moving in the opposite direction. The net result is an order of magnitude higher (than the symmetric case) gas velocity downstream of the right edge of the exposed anode with a two orders of magnitude smaller negative velocity near the left edge [see Fig. 3(d)]. These solutions agree with the experimental findings[27] of the existence of a low pressure region in the plasma and flow induction by both symmetric and asymmetric plasma actuators. Also, the experiments in Ref. 27 show a peak velocity 1 mm above the exposed electrode which matches with the numerical prediction. Simulation re-

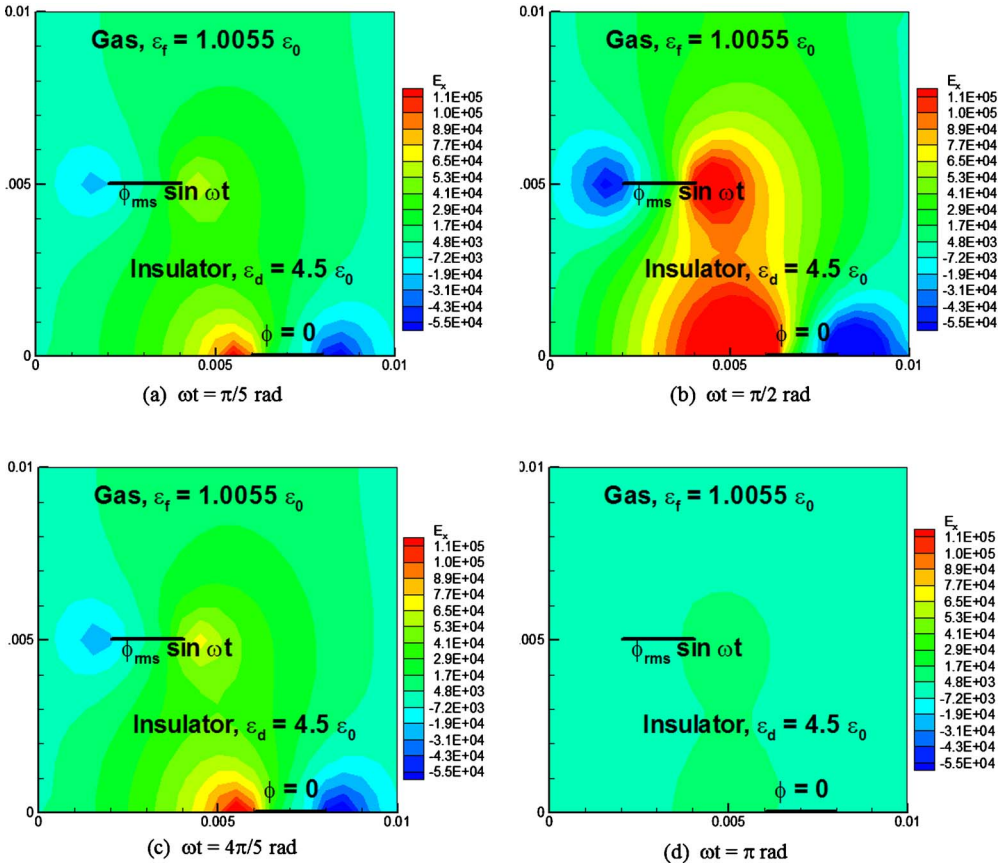

FIG. 4. (Color online) Time evolution of computed axial electric field (volts/cm) distribution in the computational domain.

sults highlight that the asymmetry enhances the electric field and thus influences flow direction.

A clearer understanding of the asymmetric configuration S-2 may be derived by exploring various quantities at several phases of the excitation. The time evolution of the potential distribution, axial electric field, charge distribution, and streamwise and crosswise electron current components are shown in Figs. 4–6 for four time stations inside a half cycle. The axial electric field in Fig. 4 shows the development of a near-circular growth of positive peak of approximately 1.1×10^5 V/cm and negative trough of 5.5×10^4 V/cm at the right and left end of the exposed electrode, respectively. The computed solutions are very similar to the experimental data of Corke *et al.*[3] and Roth *et al.*,[27] where the exposed electrode is situated upstream of the peak location of the electric field and thus the peak of velocity. Note that the highest value of the electric field about the edges of the grounded electrode is at least twice as much of that near the exposed electrode. The peak of the crosswise component E_y (not shown here due to space limitations) is, however, just above the electrodes. Specifically, above the positive electrode E_y takes values of about 4×10^4 V/cm.

Based on the Poisson equation (2), the divergence of the electric field is directly related to the charge distribution. The nonuniform nature of the distribution along the edge of the dielectric is further elucidated in the two-dimensional charge solutions plotted in Fig. 5. Note that a residual negative charge remains deposited on the dielectric surface downstream of the exposed electrode for the entire duration of the cycle. This causes a net electric force in the direction from the electrode to the downstream surface. This is the fundamental reason why the net near-wall jet velocity is unidirectional. The negative charge accumulation at the surface is consistent with the physical model of the DBD for the charge deposition at the surface of the dielectric.[5]

Figure 6 displays the peak streamwise electron current (+2.4, −4.1 mA) observed at the two corners (right and left) of the exposed electrode with a peak value of −28.1 mA at π radians, and the minimum current (+0.3, −0.1 mA) is computed at $\pi/2$ radians of the phase. An explanation for this behavior may be proposed based on arguments pertaining to the observed self-limiting nature of the discharge. In surface DBD there is no real current path between the electrodes. However, the charge buildup on the insulator surface opposes the applied voltage, shutting off the discharge just beyond the peak when the applied voltage starts decreasing, thus self-limiting the system. This is also confirmed by the experimental data (see, for example, Fig. 2 of Ref. 17), where the current magnitude peaks at about π radians. The local fluctuations above the rf electrode as seen in Fig. 6(b) show a possible electrical double layer about the sheath edge. The crosswise electron current in Fig. 8 also shows similar surface characteristic with low currents at $\pi/2$ radian and large peak value (−243 mA) near π radian.

Figure 7(a) plots the streamwise component of the com-

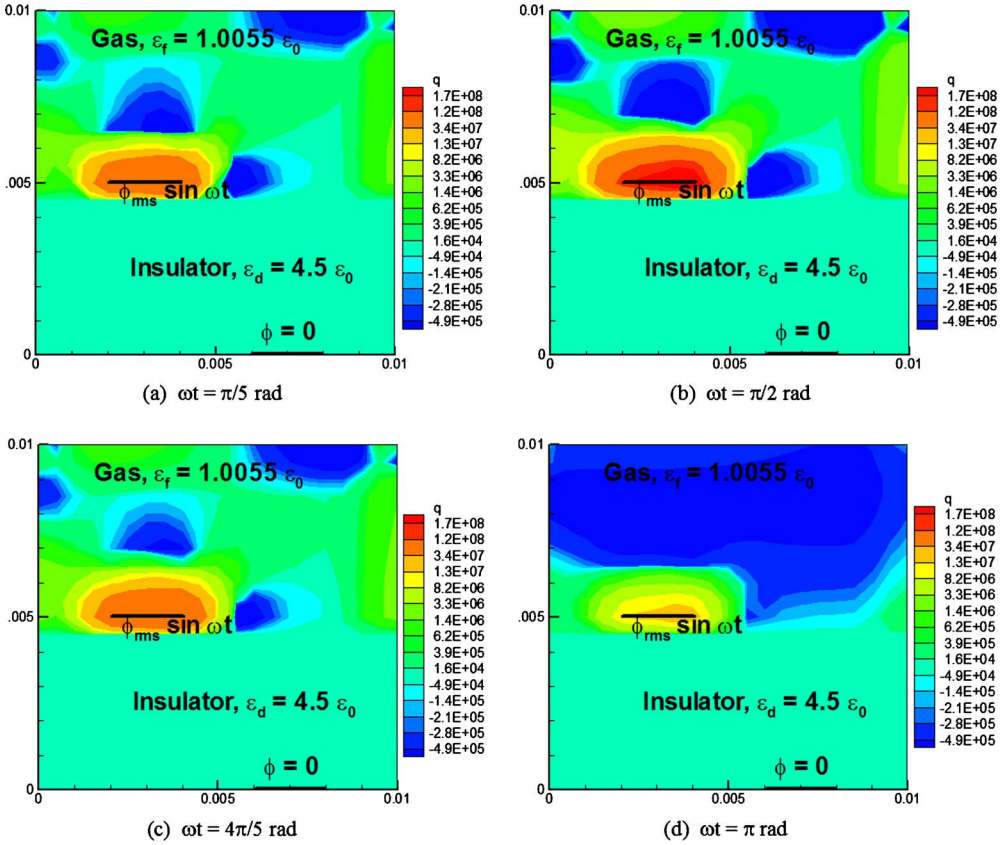

FIG. 5. (Color online) Time evolution of charge $(n_i - n_e)$ distribution in the computational domain.

puted gas velocity depicting a strong peak downstream of the rf electrode away from the dielectric surface. The initial condition is zero flow, which makes the computational problem more challenging. The local vertical line plots at seven streamwise locations describe how the flow velocity increases in response to the increase in axial electric field (Fig. 3). The peak of the wall jet like feature occurs at ~2 mm downstream of the exposed electrode, beyond which diffusive momentum transfer increases the height of the region influenced by the DBD, and the peak velocity diminishes. The velocity induced by the discharge is relatively small, but should increase if the interelectrode gap is decreased in both vertical and streamwise directions as that will increase the magnitude of the force generated by the electric field. In Refs. 2 and 4, it has been conjectured that it is the Lorentzian collision between the ions and neutrals that brings about the plasma-to-gas momentum transfer. Our results, in fact, indicate that for helium the electron-neutral collisional influence $m_e n_e \nu_{en}(V_{ej} - V_{nj})$ in this process may not be negligible as compared to the effect of ion-neutral collision, $M n_i \nu_{in}(V_{ij} - V_{nj})$. It is because $M \gg m_e$ and $n_i \nu_{in} V_{ij} \ll n_e \nu_{en} V_{ej}$ results in $m_e n_e \nu_{en} V_{ej} \sim M n_i \nu_{in} V_{ij}$.

For future design purposes, it is important to understand the effect of permittivity of the dielectric material on the electric field and thus on the flow control. Figure 8 shows the effect for two different dielectric constants that are orders of magnitude apart (although realistic materials have dielectric constants below 10, we intend to amplify the effect). The encircled region about the insulator surface highlights the observation that, as the dielectric constant increases, the crosswise electric field decreases noticeably, bending the electric field lines almost parallel to the surface. This increases the current component, due to higher resistivity in the electric path resulting in higher power requirement. More investigations are required to confirm this inference.

The analyses of R-1 and R-2 are reported in Figs. 9–12. In general, the electrohydrodynamic (EHD) body force calculated based on the product of charge and electric field shows very strong forward and downward moving vectors downstream of the exposed electrode for the positive part of the cycle. At the negative peak of the cycle, the force vectors concentrate just upstream of the right edge of the powered electrode with majority forces going backward and downward. However, for the rest of the cycle the force is much smaller as compared to the positive part (~10%, 42%, and 2% of the peak magnitude, respectively, at π, $3\pi/2$, and 2π radians). The average body force will thus push the bulk gas in the forward and downward directions. Recent numerical simulation[6,7] documented the gas velocity downstream of the right edge of the exposed anode with a two orders of magnitude smaller negative velocity near the left edge of the exposed electrode similar to what we observe here.

Figure 9 plots the streamwise component of the time average of volume specific body force for case R-1. The line trace of the force vectors is showing a directional bifurcation (similar to that reported in a recent PIV experiment,[28] Fig. 2) just downstream of the exposed electrode. This will tend to guide the flow in both directions at just about $x = 2$ cm loca-

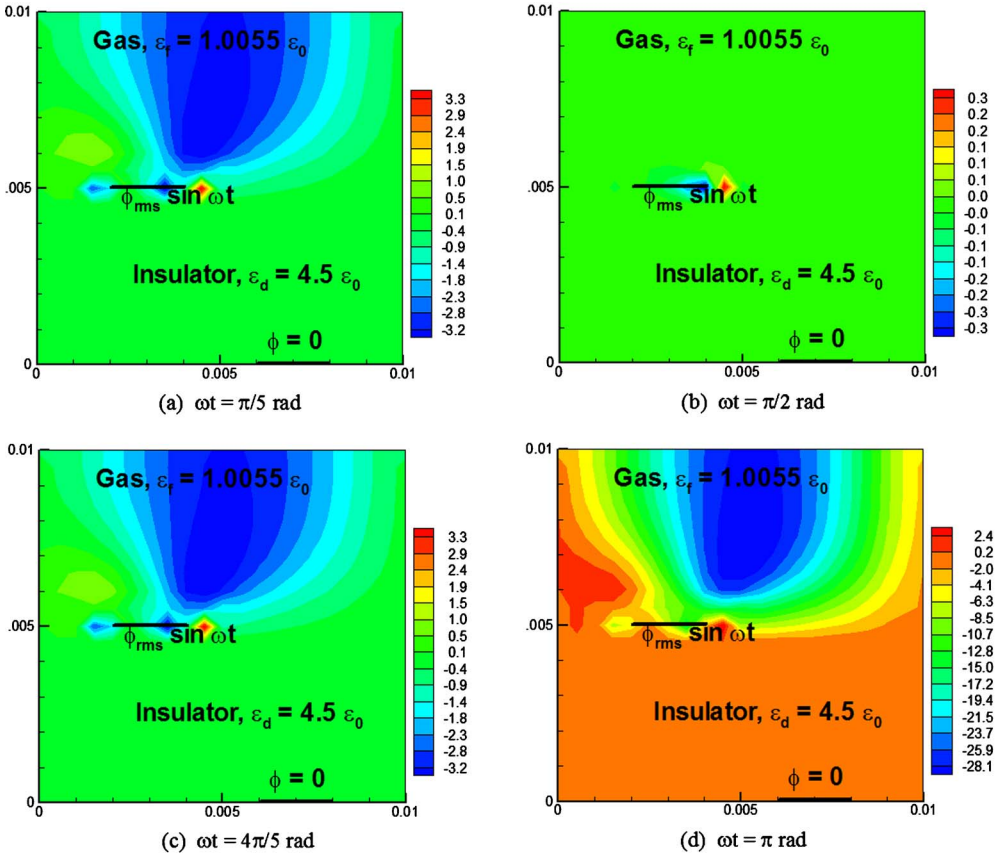

FIG. 6. (Color online) Time evolution of streamwise component of the electron current in mA.

tion. The positive peak very close to the dielectric surface is three times higher than the negative peak. Due to fluid inertia, the bulk gas will only respond to this average force, which will ensure its net forward motion. The momentum thus imparted to the gas will induce a velocity along the dielectric surface. Figure 10 plots the streamwise component of the gas velocity computed from Eq. (4) for case R-1 at six local vertical line plots upstream and downstream of the electrode edge and shows a wall jet like feature. The zero flow initial condition makes the computational problem more challenging. The peak of this wall jet of 2.4 m/s occurs at 6 mm downstream of the exposed electrode, beyond which diffusive momentum transfer increases the height of the region influenced by the DBD, and the peak velocity diminishes. Similar velocity profiles have been observed by several experimental groups.[1–4,27,28] Note that for helium gas at 300 Torr the mobility is much higher than atmospheric air and hence the predicted induced velocity is higher.

Specific details of gas velocity components and the streamwise force is presented in Fig. 11 at five locations along the dielectric at $t=6$ ms. It is interesting to note that the peak force is located at $x=0.7$ cm in the middle of the initial bubble, while the peak of the wall jet is occurring downstream of the exposed electrode at $x=2.0$ cm. The location of the actuator is thus important to control the flow effectively.

For the actuator model to work for design purposes, it is essential to test it for low speed flow conditions where a reasonable amount of supporting experiments have been reported. Figure 12 shows the transient effect of DBD actuator for realistic gas flow control. The time scale of gas flow for the present dimensions is in milliseconds while the plasma time scale is several orders of magnitude less. For this case R-2 simulation, first an initial flow condition is generated over the flat plate kept at a 12 deg angle with respect to the helium gas inflow without the rf power turned on. Figure 12(a) plots the stream traces of gas particles based on the velocity vectors of the initial flow field and shows a strong separated flow (see the inset) just downstream of the leading edge of the plate. Then, the power is turned on for the same electrode arrangement as presented earlier. Figures 12(b)–12(d) show the gradual removal of the recirculation bubble due to the separation as a function of time. The strong positive force contours (in red) shows the time average dynamics of the streamwise component as it literally pushes the recirculation off the plate within 6 ms. The fluid reacts to the generated mean body force but there may be a slow interaction with the local plasma generation as time progresses. To our knowledge, such description has not been shown in the reported literature to date.

V. CONCLUSIONS

A two-dimensional finite-element-based formulation of plasma-fluid interactions is given for a partially ionized plasma using the multicomponent fluid equation. The model is applied to simulate an atmospheric surface dielectric barrier discharge for partially ionized helium gas. The computed

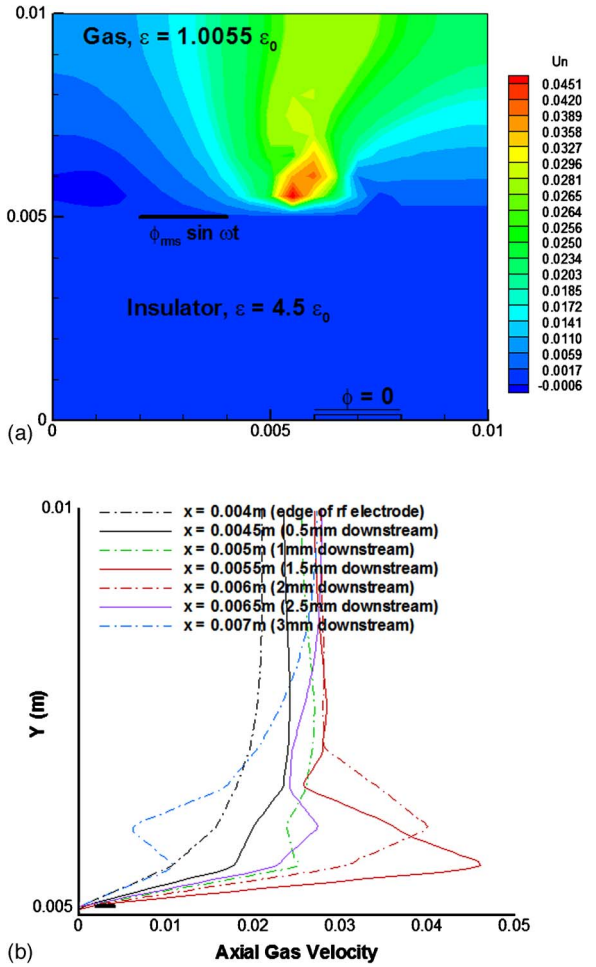

FIG. 7. (Color online) (a) Contours of the streamwise velocity identify the location of highest momentum transfer. (b) Calculated streamwise component of the gas velocity distribution at different locations along the flow showing similar wall jet as found in experiments (Refs. 3, 4, and 28).

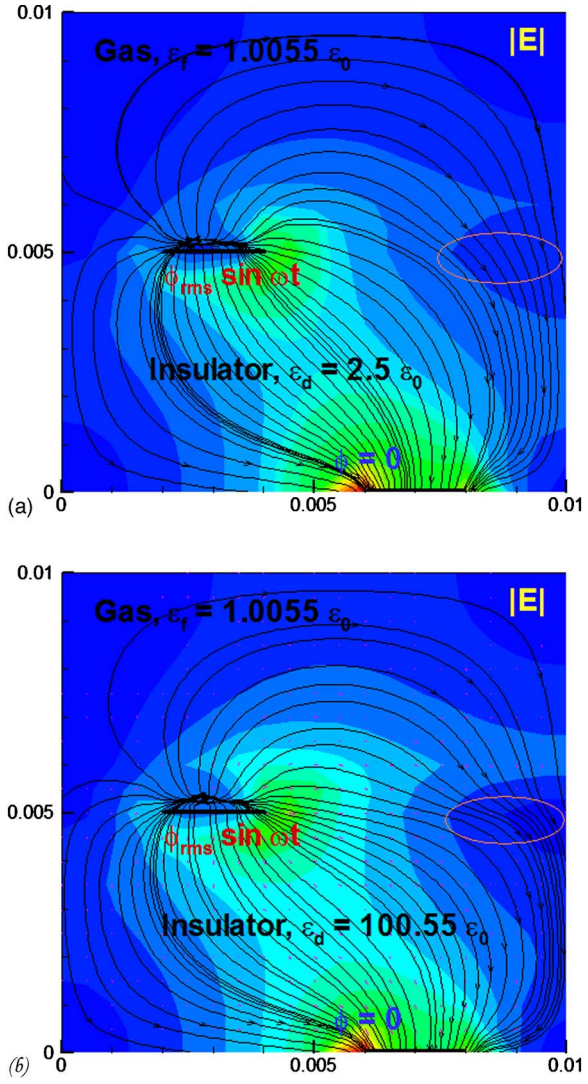

FIG. 8. (Color online) The electric field lines show as the dielectric constant increases the field lines at the surface of the dielectric bend in the highlighted ellipse, showing possible increase in current, hence the power requirement.

results are similar to the experimental data showing that the exposed electrode is situated upstream of the peak location of the electric field and thus the imparted momentum. The two-dimensional predictions mimic the self-limiting discharge mechanism due to the charge accumulation on the insulator surface and the lowest electron current just beyond the peak applied voltage. The results, however, stress that the asymmetry enhances the electric field. The effect of increasing insulator dielectric constant in the computed electric field lines shows noticeable decrease in the crosswise electric field, possibly increasing the power requirement. More investigation is needed to ascertain optimum electrical and geometric design parameters. In our simulations, the electric field varies, but reaches a quasiperiodic asymptote. The fundamental reason for the net near-wall unidirectional jet velocity can be explained as electrostatic force along the electric field toward the electron deposition downstream. The issue of whether the fluid reacts to this force in a mean or time-varying sense has not yet been resolved, and requires future work. Also, we have utilized 300 Torr pressure while the atmospheric pressure is nearly 2.6 times higher. This will increase the collisional effects, reducing charge mobility and decreasing resulting induced momentum transfer to the gas.

In the near future, the model will be extended to atmospheric air with negative ions and additional new mechanisms in the source terms. A model for realistic, fully three-dimensional geometric and electrode configuration is also in develop-

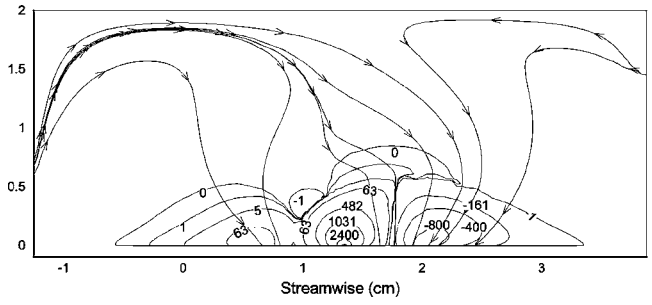

FIG. 9. Time average of streamwise component of the μN force per unit volume about the surface of the actuator shows the dominance of the streamwise forward (positive) force component. Line traces show the direction of force which will guide the local flow.

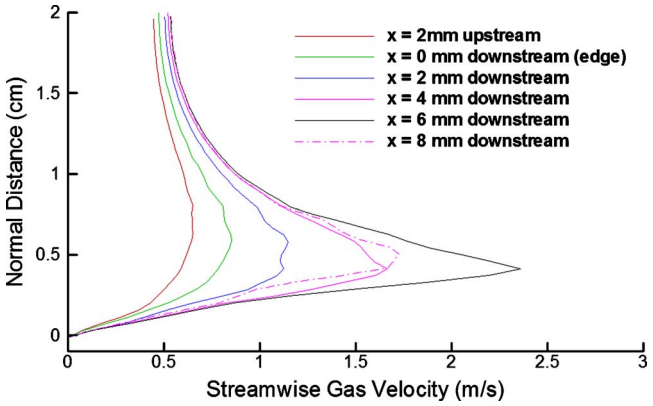

FIG. 10. Computed streamwise velocity induced in a quiescent helium gas.

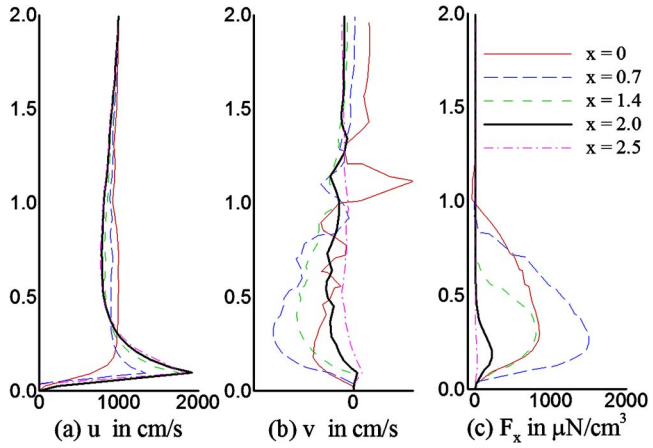

FIG. 11. Velocity components and streamwise volume specific force distribution at specific locations (x in cm) normal to the dielectric surface after 6 ms.

ment, as is an exploration of the effect of different voltage shapes (e.g., sawtooth, square wave, etc.). The present effort thus provides a practical tool to augment experimental observations in exploring flow control concepts and in developing suitable inputs for traditional fluid dynamics codes based on the Navier-Stokes equations.

A. Major future advancements needed

The electron temperature was assumed to be uniform at T_e=1 eV. This assumption can lead to substantial errors. In fact, at these high pressures (~300 Torr) the characteristic relaxation time of electron temperature is on the order of 3 nanoseconds; accordingly, the relaxation length is also very short. Therefore, T_e is a function of the local value of E/N. Since E is quite nonuniform, T_e is also quite nonuniform. One immediate consequence is that considerable gradients of T_e should result in additional electron fluxes. In Eq. (1b), the diffusion term only has the gradient of electron density. However, the diffusion term should in general be proportional to the gradient of electron pressure and can be broken into two terms—one with electron density gradient, and the other with the electron temperature gradient.

(2) Also, electron adsorption on the dielectric surface occurs for a dielectric coated anode. The electron avalanches flood the dielectric surface until the threshold intensity is attained for formation of streamers. For applied rf voltage, thermo-desorption and interaction with vibrationally excited and metastable gas molecules may cause the electron emission from the dielectric and electrode surfaces. Maslov

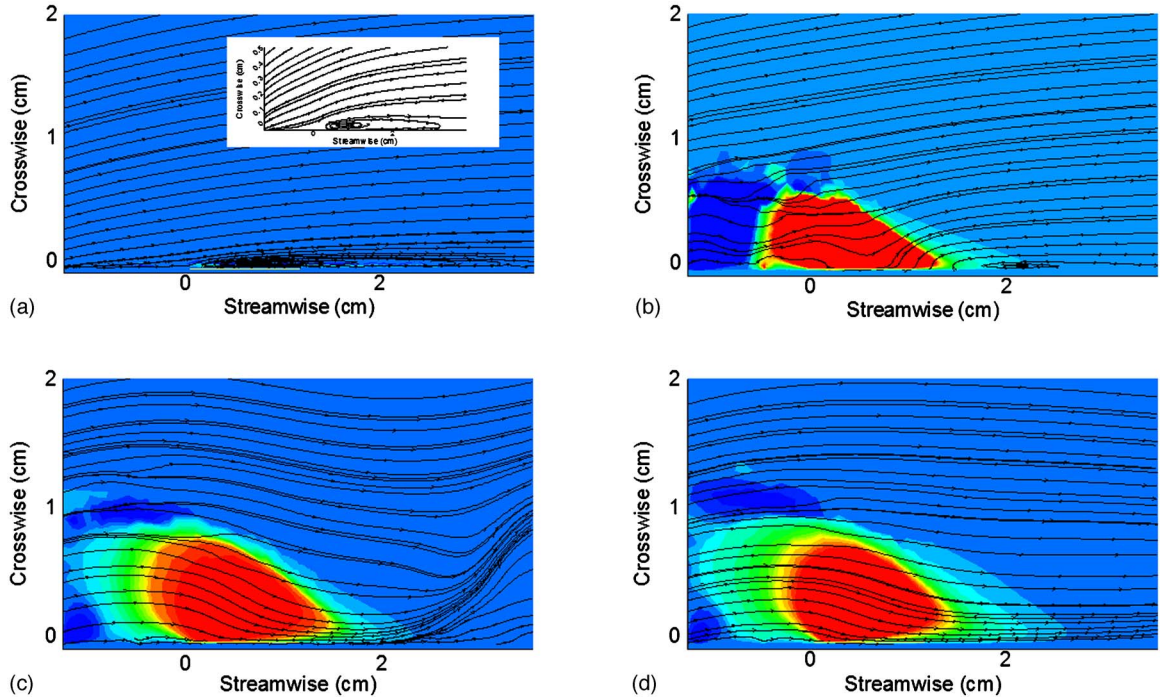

FIG. 12. (Color online) Separation control for an incoming flow with +12° AOA over a flat plate shows the gradual flow attachment eradicating the separation bubble in a few milliseconds. The velocity stream traces are plotted over the streamwise specific force contours showing a strong average force over the exposed electrode.

et al.[29] conjectured that the secondary electron emission due to ion current seems to be less important than the aforementioned mechanisms. However, the electrons emitted from the surface become the source for electron avalanche development and their further transformation into streamers. Thus for completeness, the modality of plasma-wall interaction should be carefully investigated.

ACKNOWLEDGMENTS

The authors acknowledge help from K. P. Singh and Haribalan Kumar in preparation of this paper.

This work was partially supported by the AFOSR Grant No. FA9550-05-1-0074 monitored by John Schmisseur and the Air Force Research Laboratory Contract No. F33615-98-D-3210 and the National Academy of Science NRC/AFOSR research fellowship during the summer of 2004.

[1] J. R. Roth, U.S. Patent No. 5,669,583, 23 September 1997.
[2] J. R. Roth, *Industrial Plasma Engineering. Volume II—Applications to Non-Thermal Plasma Processing* (Institute of Physics, Bristol, 2001), Sec. 18.6.
[3] T. C. Corke, E. J. Jumper, M. L. Post, D. Orlov, and T. E. McLaughlin, *40th AIAA Aerospace Sciences Meeting*, Reno, 2002 (AIAA, Washington, DC, 2002), Paper No. 2002-0350.
[4] J. R. Roth, Phys. Plasmas **10**, 2117 (2003).
[5] C. L. Enloe, T. E. McLaughlin, R. D. VanDyken, K. D. Kachner, E. J. Jumper, and T. C. Corke, AIAA J. **42**, 595 (2004).
[6] T. Corke and M. Post, *Proceedings of 43rd Aerospace Sciences Meeting*, Reno, 2005 (AIAA, Washington, D.C., 2002), Paper No. 2005-0563.
[7] W. Shyy, B. Jayaraman, and A. Andersson, J. Appl. Phys. **92**, 6434 (2002).
[8] S. Roy and D. Gaitonde, J. Appl. Phys. **96**, 2476 (2004).
[9] S. Roy, Appl. Phys. Lett. **86**, 101502 (2005).
[10] S. Roy and D. Gaitonde, *Proceedings of 43rd Aerospace Sciences Meeting*, Reno, 2005 (AIAA, Washington, D.C., 2002), Paper No. 2005-0160.
[11] S. O. Macheret, M. N. Shneider, and R. B. Miles, J. Propul. Power **18**, 424 (2002).
[12] V. Shalaev, A. Fedorov, N. Malmuth, V. Zharov, and I. Shalaev, *Proceedings of 41st Aerospace Sciences Meeting*, Reno, 2003 (AIAA, Washington, D.C., 2003), Paper No. 2003-0034.
[13] D. Gaitonde, *Proceedings of 43rd Aerospace Sciences Meeting*, Reno, 2005 (AIAA, Washington, D.C., 2002), Paper No. 2005-0560.
[14] A. von Engle, A. Seeliger, and M. Steenback, Z. Phys. **85**, 144 (1933).
[15] A. Bogaerts, E. Neyts, R. Gijbels, and J. van der Mullen, Spectrochim. Acta, Part B **57**, 609 (2002).
[16] D. Gaitonde, M. Visbal, and S. Roy, *36th AIAA Plasma Dynamics and Lasers Conference*, Toronto, Canada, June 2005 (AIAA, Washington, D.C., 2002), AIAA Paper No. 2005-5302.
[17] F. Massines, A. Rabehi, P. Decomps, R. B. Gadri, P. Ségur, and C. Mayoux, J. Appl. Phys. **83**, 2950 (1998).
[18] K. Akhtar, J. E. Scharer, S. M. Tysk, and E. Kho, Rev. Sci. Instrum. **74**, 996 (2003).
[19] L. Ward, J. Appl. Phys. **33**, 2789 (1962).
[20] S. Roy, B. P. Pandey, J. Poggie, and D. Gaitonde, Phys. Plasmas **10**, 2578 (2003).
[21] D. Balagangadhar and S. Roy, Comput. Methods Appl. Mech. Eng. **190**, 5465 (2001).
[22] S. Roy and B. P. Pandey, J. Propul. Power **19**, 964 (2003).
[23] S. M. Cooper, B. A. Cruden, M. Meyyappan, R. Raju, and S. Roy, Nano Lett. **4**, 377 (2004).
[24] R. Raju and S. Roy, J. Thermophys. Heat Transfer **19**, 106 (2005).
[25] J. N. Reddy, *An Introduction to the Finite Element Method* (McGraw-Hill, New York, 1984).
[26] M. Riser, Comput. Methods Appl. Mech. Eng. **2**, 65 (1972).
[27] J. R. Roth, D. M. Shermanand, and S. P. Wilkinson, *Proceedings of the 36th AIAA Aerospace Sciences Meeting & Exhibit* Reno, NV, January 12–15, 1998 (AIAA, Washington, D.C., 2002), AIAA Paper 98-0328.
[28] J. Jacob, K. Ramakumar, R. Anthony, and R. Rivir, Fourth Int. Symposium on Turbulence and Shear Flow Phenomena, No. TSFP4-225, June 2005.
[29] A. Maslov, B. Zanin, A. Sidorenko, V. Fomichev, A. Pavlov, and B. Postnikov, in *Proceedings of the 42nd AIAA Aerospace Sciences Meeting & Exhibit*, Reno, NV, 2004 (AIAA, Washington, D.C., 2002), Paper No. 2004-0843.